

Article

Synergistic Effect of Phase Transformation and Stress-Induced Twinning on the Antibacterial Property and Elastic Modulus of Ti-13Nb-13Zr-7Ag

Diangeng Cai ^{1,2}, Jiayu Wang ^{1,2}, Lei Yang ^{1,2}, Xiaocen Xu ¹ and Erlin Zhang ^{1,2,*}

¹ Key Laboratory for Anisotropy and Texture of Materials, Education Ministry of China, School of Materials Science and Engineering, Northeastern University, Shenyang 110819, China

² Research Center for Metallic Wires, Northeastern University, Shenyang 110819, China

* Correspondence: zhangel@atm.neu.edu.cn; Tel./Fax: +86-024-8368-9400

Abstract: Ti-13Nb-13Zr-7Ag (TNZ-7Ag) has a great potential for biomedical application due to its low elastic modulus and excellent antibacterial properties. However, it is difficult to balance low elastic modulus and high antibacterial properties. In this study, the TNZ-7Ag was treated by a pre-deformation and aging treatment to avoid this problem. The results proved that the stress-induced twinning caused a large range of Ti₂Ag particle agglomeration, and in turn enhanced the antibacterial performance of Ag-containing titanium alloys. And the twinned martensite formed during the pre-deformation promoted the precipitation of Ti₂Ag phase and inhibited the growth of α phase. As a result, TNZ-7Ag with both low elastic modulus and strong antibacterial properties was obtained by the treatments. All results demonstrated that pre-deformation based on the synergistic effect of aging treatment was an effective strategy to develop novel biomedical titanium alloys. Low-elastic-modulus antibacterial titanium alloys, which can be used for the development of novel biomedical titanium alloys, were prepared.

Keywords: Ti alloys; pre-deformation; aging treatment; antibacterial metals; elastic modulus



Citation: Cai, D.; Wang, J.; Yang, L.; Xu, X.; Zhang, E. Synergistic Effect of Phase Transformation and Stress-Induced Twinning on the Antibacterial Property and Elastic Modulus of Ti-13Nb-13Zr-7Ag. *Metals* **2024**, *14*, 901. <https://doi.org/10.3390/met14080901>

Academic Editor: Silvia Spriano

Received: 11 July 2024

Revised: 31 July 2024

Accepted: 6 August 2024

Published: 8 August 2024



Copyright: © 2024 by the authors. Licensee MDPI, Basel, Switzerland. This article is an open access article distributed under the terms and conditions of the Creative Commons Attribution (CC BY) license (<https://creativecommons.org/licenses/by/4.0/>).

1. Introduction

Antibacterial titanium alloys, including Ti-Ag/Ti-Cu alloys, have attracted widespread attention in the field of biomedical applications, especially in bone implants, due to their excellent antibacterial properties, corrosion resistance, and cell compatibility [1–3]. As an additive element for alloys and composites applications, Ag has the advantage of broad-spectrum antibacterial activity and a lower likelihood of developing drug-resistant strains than Cu [4,5]. Therefore, Ag-containing antibacterial titanium alloys represent a promising choice for biomedical materials [6,7]. As a biomaterial for implants, another crucial aspect under consideration is the mismatching in the elastic modulus between Ti alloys and human bones [8]. To reduce the mismatch and increase the service life of the titanium implants, researchers have been trying to develop biomedical titanium alloys with low elastic modulus [9] by tuning the phase composition, aiming to preserve low-modulus phases (such as β , α'') as much as possible, while minimizing the presence of high-modulus phases (such as α , ω) [10].

Recently, Ag-containing near- β/β titanium alloys have been developed to satisfy both antibacterial performance and low-elastic-modulus requirements, such as Ti-13Nb-13Zr-xAg [11], Ti-15Mo-xAg [12], and Ti-30Nb-Ag [13,14]. With the advancement of Ag-containing near- β titanium alloys, there has been a deeper understanding of the relationship between the antibacterial performance and microstructure. Existing studies indicate that the Ag-containing near- β Ti alloys have significantly superior antibacterial ability than Ti-Ag binary alloys with the same amount of Ag addition due to the different distribution of Ti₂Ag precipitation caused by the martensitic phase transformation [11,15]. In Ti-Ag binary

alloys, Ti₂Ag phase uniformly precipitates within α -phase grains [15]. However, in Ag-containing β -type Ti alloys, Ti₂Ag phase is distributed in localized Ag-rich areas, forming regions with high-density Ti₂Ag particle precipitation [13]. This suggests that metastable phase transformations with Ag segregation might be advantageous for enhancing the antibacterial performance of Ag-containing Ti alloys.

Aging is a common heat treatment in antibacterial Ti alloys. The aging temperature is close to the eutectoid temperature of Ti₂Ag phase and the martensitic temperature in Ag-containing near- β Ti alloys [13]. In the case of Ag-containing near- β titanium alloys, there are two phase transformation processes during the aging treatment, $\beta \rightarrow \alpha + \text{Ti}_2\text{Ag}$ and $\beta \rightarrow \alpha''$. As mentioned earlier, introducing martensitic transformation into the aging process can simultaneously reduce the elastic modulus of the material and enhance its antibacterial properties. However, the precipitation of α phase decreases the effect of the α'' phase on lowering the elastic modulus. For example, in Ti-13Nb-13Zr-xAg, the elastic modulus was 75 GPa after solution and water-quenching treatment, while it increased to over 90 GPa after being aged at 600 °C, which was obviously due to the precipitation of α phase [13]. Therefore, it is necessary to avoid the precipitation of the α phase and promote the precipitation of the α'' phase, while few studies have been conducted on avoiding the increase in elastic modulus of titanium alloys during the aging process. At the same time, studies have shown that by controlling the proportion of α'' and β phases in titanium alloys, the elastic modulus can be reduced and the increase in it with temperature can be suppressed [16]. Inspired by this point, this study applied pre-deformation to Ti-13Nb-13Zr-7Ag before aging to lead to the decomposition of the metastable β phase in near- β titanium alloy into $\alpha'' + \beta$ phases under stress induction and to avoid the precipitation of the α phase, thereby increasing the proportion of the α'' phase and reducing the elastic modulus while retaining high antibacterial properties.

Considering the role of the martensitic phase in promoting the precipitation of antibacterial phases, it is possible to obtain a large amount of Ti₂Ag phases and increase the percentage of martensitic phases by means of pre-deformation + aging, in turn obtaining titanium alloy with low elastic modulus and high antibacterial activity. Additionally, this method can simultaneously introduce stress-induced twins, whose internal stresses also have a promoting effect on the precipitation of antibacterial phases [17].

Therefore, this study applied a pre-deformation + aging approach to Ti-13Nb-13Zr-7Ag (TNZ-7Ag) to clarify the synergistic effect of martensite and stress-induced twinning on the antibacterial property and elastic modulus. The primary results showed that the TNZ-7Ag obtained a high antibacterial rate of over 95% and a low elastic modulus of 75 GPa with the pre-deformation + aging process, which demonstrated the great potential of a pre-deformation process in the preparation of antibacterial titanium alloys with low elastic modulus.

2. Experimental

2.1. Material Preparation

Ti-13Nb-13Zr-7Ag (TNZ-7Ag) was prepared by a non-self-consumption vacuum arc melting furnace with Ti-50Nb master alloy, high-purity Ag (99.9), sponge Ti (99.1–99.7), and sponge Zr (99.1–99.7) as raw materials. The ingots were melted 6 times in an atmosphere with a vacuum of 2.0×10^{-3} Pa. The chemical composition (wt%) tested by EDS is listed in Table 1. The ingots were forged into plates and kept at 850 °C for 2 h, and then quenched by water, named T4. Then the plates were rolled with a deformation of 20–50% at room temperature as pre-deformation. The samples pre-deformed with 50% deformation was aged at 600 °C for 0.5 h, 1 h, 1.5 h, and 2 h, named as 50%/0.5 h, 1 h, 1.5 h, and 2 h, respectively.

Table 1. The chemical composition of TNZ-7Ag.

Element	Nb	Zr	Ag	Ti
Composition/wt%	13.2	12.8	6.5	Balanced

2.2. Phase Identification

The X-ray diffractometry (XRD) was carried out on a SmartLab. 9 (Rigaku, Japan) with a copper target to identify the phases in the samples. The instrument operated at a voltage of 40 kV and a current of 30 mA. The scanning speed was set to 4°/min, covering a range of 30–90°.

2.3. Microstructure

The materials were cut from plates into samples with a diameter of 15 mm and a thickness of 2 mm with wire cutters. They were then ground with 3000 mesh sandpaper and polished using a 1.5 µm diamond solution. Following this, etching was performed with Kroll's reagent in a volume ratio of HF:HNO₃:H₂O = 4:14:82. The microstructure was analyzed using a field emission scanning electron microscope (Ultra Plus, Zeiss, Oberkochen, Germany). For transmission electron microscopy (JEM-2100F, JEOL Corporation of Japan, Tokyo, Japan), samples were prepared as flakes with a 3 mm diameter and 300 µm thickness. These flakes were ground to a thickness of 50–70 µm using 2000 mesh sandpaper and then subjected to electrolytic double-spraying with a Tenupol-5 in 5% perchloric acid alcohol at 30 V and −25 °C.

2.4. Antibacterial Properties

The antibacterial properties were tested by the plate count method according to GB/T 2591. *Staphylococcus aureus* (ATCC 6538) was selected for the experiment, and commercial pure titanium (cp-Ti) was used for the control group. All glassware and samples were sterilized in an autoclave for 30 min (at 121 °C and 0.15 MPa). The samples were then placed in well plates. The bacterial solution was initially diluted tenfold with beef broth nutrient solution, followed by another tenfold dilution with 0.9% NaCl solution to achieve a concentration of 10⁵ cfu/mL. A 100 µL aliquot of this diluted bacterial solution was added to each sample surface. Then the samples with the bacterial solution were incubated at 37 ± 0.5 °C with 90% humidity for 24 h. Subsequently, 2 mL of normal saline was added to each well and shaken for 5 min. A 100 µL portion of the bacterial solution was then inoculated onto nutrient agar medium and cultured for another 24 h under the same conditions. Finally, the numbers of colonies (N) were obtained from the surface of the medium, and the antibacterial rate (R) was calculated using the following formula:

$$R = \left(1 - \frac{N_{\text{Samples}}}{N_{\text{Control}}} \right) \times 100\%$$

where N_{Samples} and N_{Control} are the number of colonies on the experimental samples and the control samples.

2.5. Elastic Modulus

The elastic modulus was evaluated by the Dynamic Property Tester for Solid Materials (China Building Materials Inspection and Certification Center) according to the national standard (GB/T 31544-2015) [18]. Three rectangular samples with dimensions of 48 mm × 10 mm × 2 mm were used.

2.6. Corrosion Resistance

Corrosion resistance was evaluated using a laboratory automated corrosion testing system (Versa STAT v3-400, Applied Research Institute, Princeton, NJ, USA) in simulated body fluid (SBF) solution at 37 ± 0.5 °C. The chemical composition of SBF solution was: NaCl, 8.00 g/L, KCl, 2.00 g/L, CaCl₂, 0.14 g/L, NaHCO₃, 0.35 g/L, MgSO₄·7H₂O, 0.20 g/L, Na₂HPO₄·12H₂O, 0.12 g/L, KH₂PO₄, 0.06 g/L [19]. A standard three-electrode system was employed, comprising a saturated calomel electrode as the reference electrode, a platinum electrode as the counter electrode, and the sample in the mold serving as the working electrode. The exposed working electrode surface was 0.785 cm².

The Ag ion release was determined according to the national standard GB/T 16886.12-2005 [20]. The samples were immersed for 1, 3, and 7 days in SBF solution at 37 ± 0.5 °C, maintaining a volume to surface area ratio of 2.5 mL/cm².

2.7. Cytotoxicity

The MC3T3-E1 cell line from the Cell Resource Center of Shanghai Institutes for Life Sciences was used in the experimental group, while commercially pure titanium served as the control group. The samples were immersed in minimum essential medium (MEM) with a surface area to volume ratio of 1.25 cm²/mL for 3 days to obtain the extracts, following ISO 10993-5 [21] guidelines. The extracts were then transferred to plates, and the cells were added to the extracts and co-cultured for 1, 3, and 7 days, respectively. Subsequently, 10 µL of thiazolyl blue staining solution (MTT, 5 mg/mL) was added to each well and incubated for 4 h. After removing the excess liquid, 100 µL of dimethyl sulfoxide (DMSO) was added. The plates were shaken for 15 min, and the absorbance (A) of each well was measured at 450 nm using a microplate reader. The relative growth rate (R_{grow}) was then calculated using the following formula:

$$R_{\text{grow}} = \frac{A_{\text{Sample}}}{A_{\text{Control}}} \times 100\%$$

where A_{Sample} and A_{Control} are the absorbance of the sample and control, respectively.

2.8. Statistical Analysis

All experiments were conducted in triplicate, and the quantitative statistical analysis of representative results was performed. A p -value of less than 0.05 ($p < 0.05$) was considered statistically significant.

3. Results

3.1. Microstructure after Pre-Deformation

Figure 1 shows XRD patterns of TNZ-7Ag after cold rolling with different deformations. From Figure 1a, the material before the cold rolling mainly consisted of β phase. After 20% of cold rolling deformation, α'' phase started to precipitate. When the deformation increased to 30% and 40%, the diffraction peaks of α'' phase were gradually enhanced, and the diffraction peaks of β phase were gradually reduced. After 50% deformation, the diffraction peak of Ti₂Ag phases began to appear, but only one peak could not confirm the existence of Ti₂Ag phases. As can be seen from the 50–65° local zoomed-in region in Figure 1b, after 20–40% deformation, a large amount of α'' phase precipitated in the material, but when the deformation reached 50%, the diffraction peaks of α'' phase decreased. Overall, it can be found from the XRD results that the phase transformation process in TNZ-7Ag from the initial state to the cold rolling state was: $\beta \rightarrow \alpha'' + \beta$. The deformation accelerates this phase transformation process.

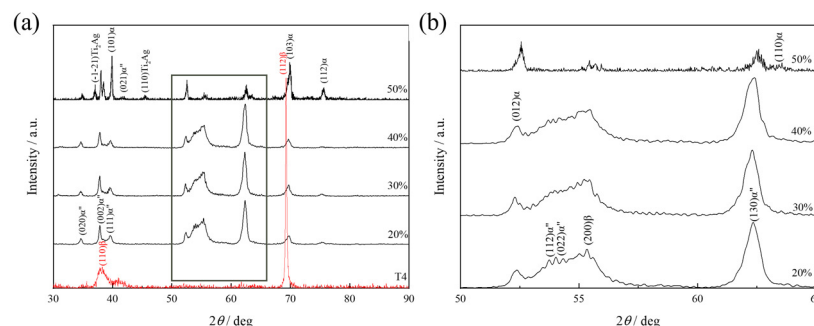


Figure 1. XRD patterns of TNZ-7Ag with different deformation. (a) XRD patterns (the T4 condition listed in red), (b) the zoomed-in region from 50–65°.

Figure 2 shows the SEM microstructure of TNZ-7Ag after room temperature cold rolling with different deformations. In Figure 2a, the α'' phase (named as $\alpha''M$) precipitated in the material after 20% cold rolling. After 30% cold rolling, the $\alpha''M$ increased and arranged in layers (Figure 2b). Then after 40% cold rolling, the $\alpha''M$ interconnected and overlapped to form a basketweave microstructure (Figure 2c). From Figure 2d, it can be found that after 50% cold rolling, the coarser lamellar martensite $\alpha''M$ precipitated in the matrix and the twin α'' phase (named as $\alpha''T$) appeared on it. Overall, the precipitated phase of TNZ-7Ag after 20–40% deformation was $\alpha''M$, while $\alpha''T$ was observed in the samples after 50% deformation.

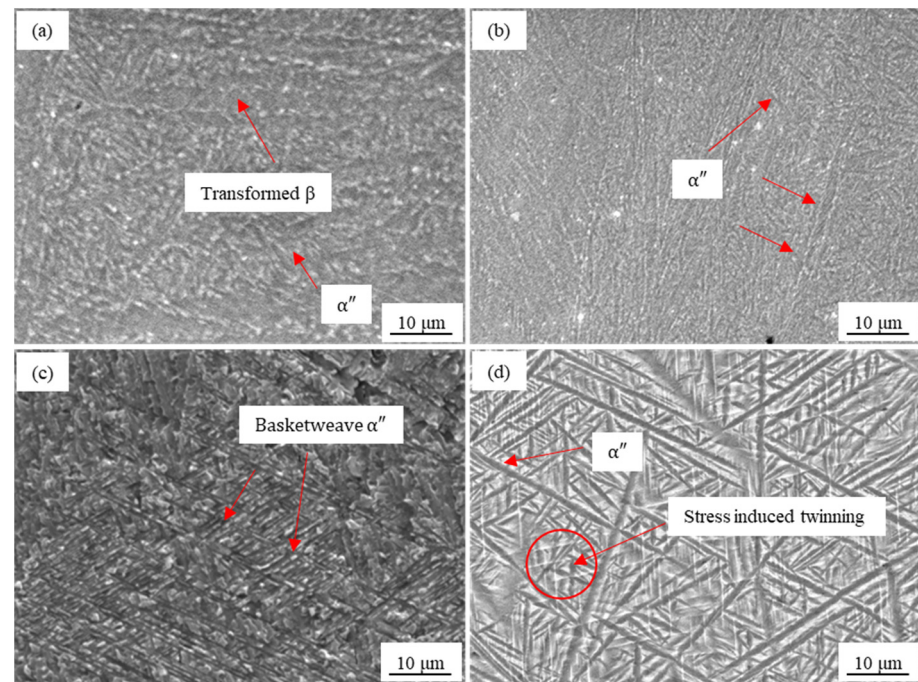


Figure 2. SEM microstructure of TNZ-7Ag with different deformation. (a) 20%, (b) 30%, (c) 40%, (d) 50%.

Figure 3 shows TEM microstructure of TNZ-7Ag after cold rolling with 50% deformation. Twins and β -phase segregation occurred in the material (Figure 3a). Firstly, based on the comparison of the bright-field image (Figure 3b) and the dark-field image (Figure 3c) made from the selected diffraction (Figure 3d) of the twin region, it can be seen that after 50% deformation, the $\alpha''T$ appeared in the $\alpha''M$, and the two types of martensite had a crystal orientation relationship $[0\bar{2}1]\alpha''M // [02\bar{1}]\alpha''T$. According to Figure 3e and the corresponding selected diffraction in Figure 3f, it can be found that in the region of β -phase separation, the crystal orientation relation of β phase and β' phase was $[011]\beta // [011]\beta'$.

To confirm the compositional distribution of the solute element clustering in Figure 3, Figure 4 shows the results of the elemental analysis performed on the sample with 50% deformation, where Figure 4a–e show the elemental mapping and Figure 4f shows the EDS analysis of the solute elements. As can be seen from Figure 4a–e, after 50% deformation, all three solute elements have undergone localized clustering, forming strips of solute-rich and solute-poor areas. As can be seen from Figure 4f, the Ag content in the solute-rich area was significantly higher than that in the solute-poor area.

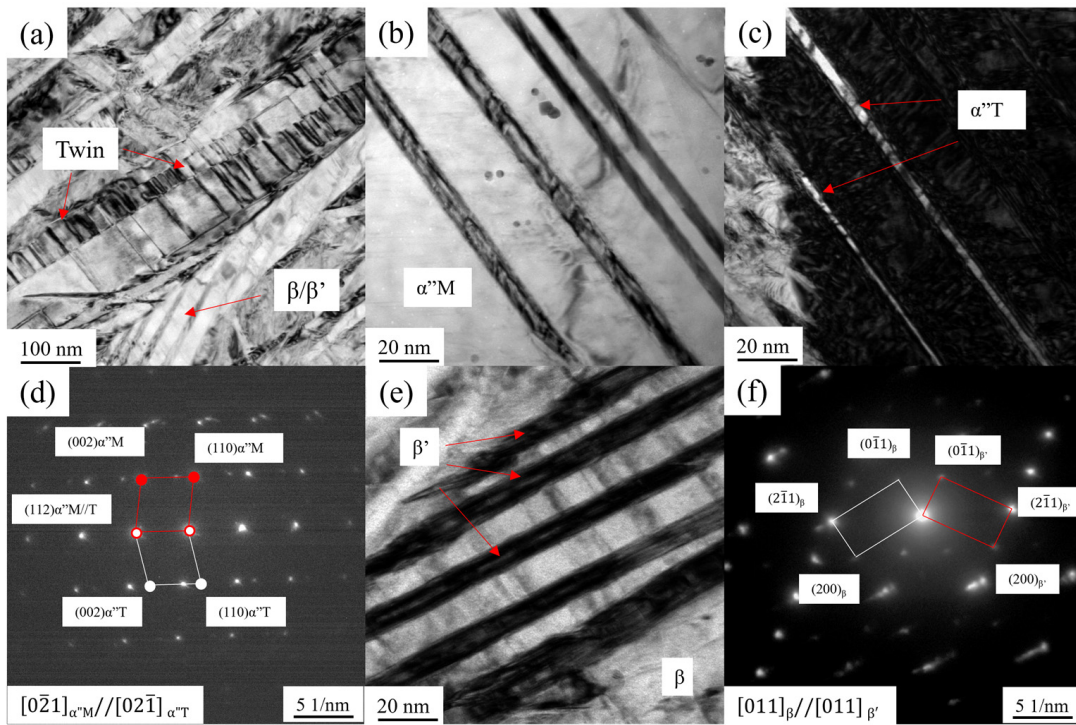


Figure 3. TEM microstructure of TNZ-7Ag with 50% deformation. (a) TNZ-7Ag with 50% deformation, (b) bright-field, (c) dark-field images and (d) SAED of twins and (e) the image and (f) SAED of β and β' phase.

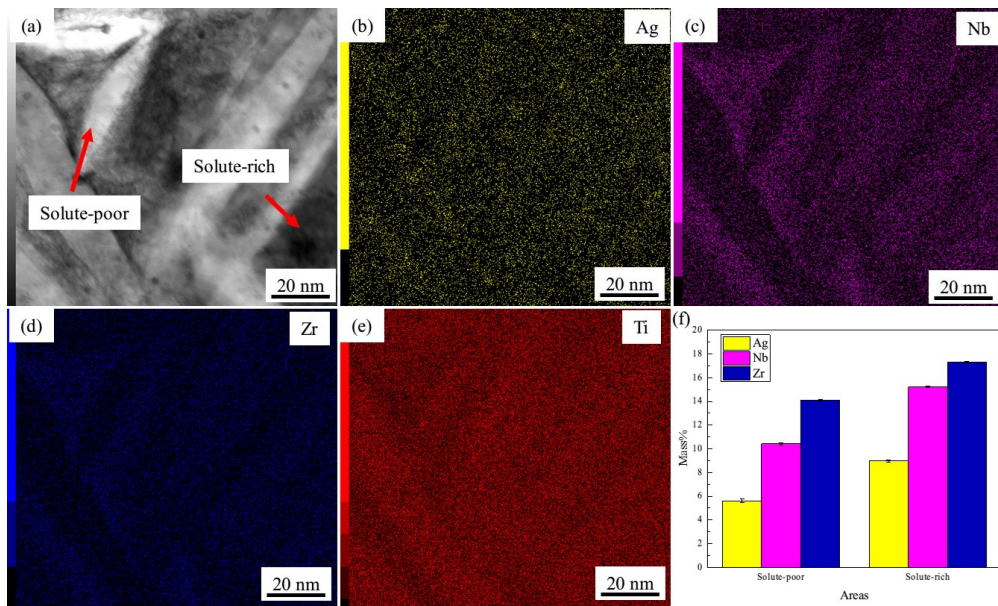


Figure 4. Element mapping and EDS results of β -phase separation. (a) STEM, (b) Ag, (c) Nb, (d) Zr, (e) Ti, (f) EDS results.

It can be summarized from the above results and analysis that the pre-deformation mainly caused $\alpha''M$ martensitic phase transformation in TNZ-7Ag alloy at the start, and with the increase in the deformation amount, the secondary martensitic phase transformation and residual β -phase segregation also took place in the alloy. The secondary martensitic phase transformation introduced the twinned martensite $\alpha''T$, while the β -phase segregation led to the localized solute clustering, which increased the local Ag concentration.

3.2. Microstructure of TNZ-7Ag with Pre-Deformation and Aging

Figure 5 shows XRD patterns of TNZ-7Ag after 50% pre-deformation and different aging durations. From Figure 5a, after being aged at 600 °C for 0.5 h, the α -phase peaks were enhanced, while β and Ti_2Ag peaks were weakened, which indicates that the amount of the α phase increased at this time. When the aging time extended to 2 h, the diffraction peaks of β were weakened and, combined with Figure 5b, a reduction in the percentage of β phase is illustrated.

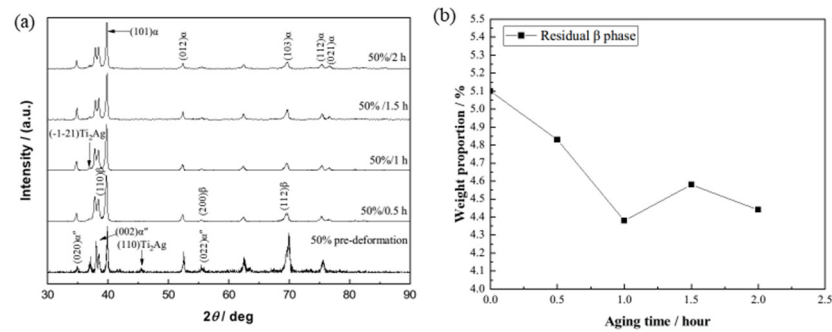


Figure 5. XRD patterns of TNZ-7Ag with 50% pre-deformation and different aging durations. (a) XRD, (b) the percentage of β phase.

Figure 6 shows the SEM microstructure of 50% pre-deformed TNZ-7Ag after 0.5–2 h of aging. According to Figure 6a,e, after 1 h of aging, the short rod-like $\alpha''\text{T}$ phases formed in the β grains, and the phase composition of 50%/0.5 h was $\alpha''\text{M} + \alpha''\text{T} + \beta$. As for Figure 6b,f, the amount of $\alpha''\text{M}$ phase decreased, while the size increased. And the number of $\alpha''\text{T}$ and Ti_2Ag phases at the nanoscale increased. According to Figure 6c,g, the amount of $\alpha''\text{M}$ phase decreased again, while the amount of $\alpha''\text{T}$ phase increased in 50%/1.5 h samples. And it is notable that there was α -phase precipitation in the $\alpha''\text{T}$ phase. When the aging time extended to 2 h, the α -phase particles became bigger, as shown in Figure 6d,h.

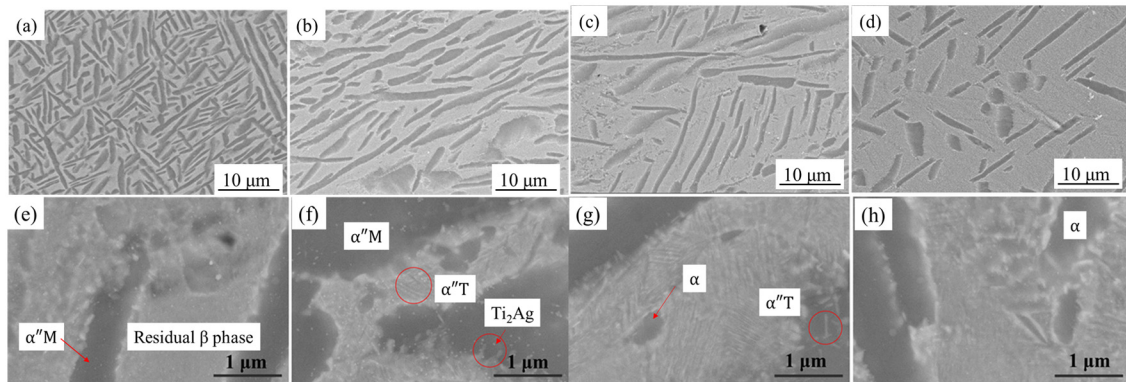


Figure 6. The SEM microstructure of TNZ-7Ag with different pre-deformation + aging treatments. (a,e) 50%/0.5 h, (b,f) 50%/1 h, (c,g) 50%/1.5 h, (d,h) 50%/2 h.

Figure 7 shows the TEM microstructure of TNZ-7Ag after different aging treatments. From Figure 7a, it can be found that the sample after 0.5 h of aging consisted of $\beta + \alpha''\text{M} + \alpha''\text{T}$, and the phase transitions were $\beta \rightarrow \alpha''\text{M}$ and $\alpha''\text{M} \rightarrow \alpha''\text{T}$, which agreed with SEM results. After 1.5 h of aging, the sample showed α phase and Ti_2Ag phase, and the $\alpha''\text{T}$ phase was also embedded in $\alpha''\text{M}$ phase, as shown in Figure 7b, which suggests that phase transformation of $\alpha''\text{T} \rightarrow \alpha + \text{Ti}_2\text{Ag}$ should occur in the $\alpha'' + \beta$ -phase region, while the $\alpha''\text{M} \rightarrow \alpha''\text{T}$ process continues. Most of $\alpha''\text{M}$ transformed into $\alpha''\text{T}$ phase after 2 h of aging, while the amount of Ti_2Ag phase increased according to Figure 7c. Combined with Figure 7d, Ti_2Ag particles were distributed in pairs for the induction of twins. High-resolution observation (Figure 7e) and Fourier transform analysis of the Ti_2Ag -phase

particles (Figure 7f,g) revealed that the Ti_2Ag particles were symmetrically precipitated because of the introduced α'' T phase.

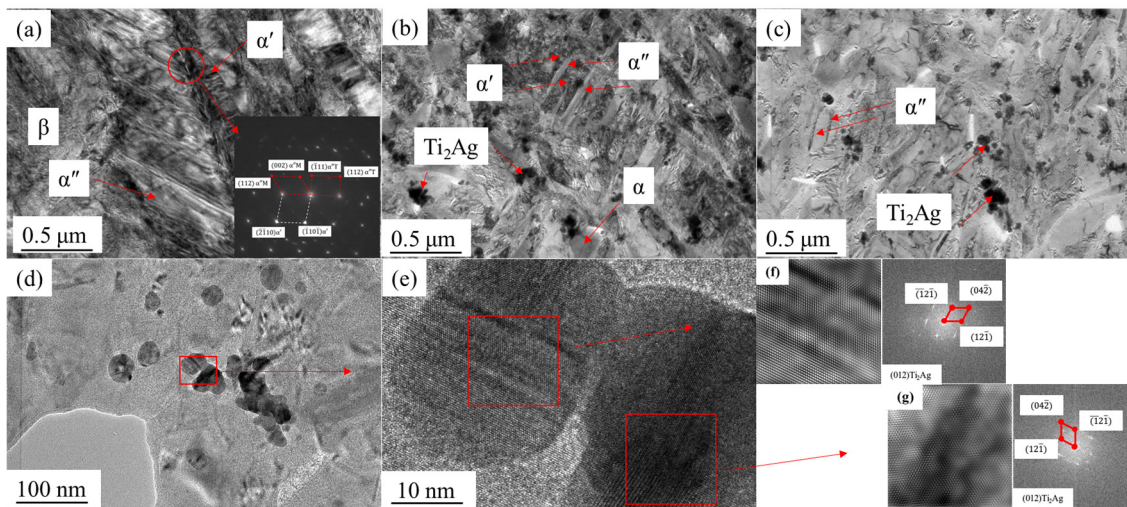


Figure 7. TEM microstructure of TNZ-7Ag with 50%-deformation + 600 °C aging treatments. (a) 50%/0.5 h, (b) 50%/1.5 h, (c) 50%/2 h, (d,e) high-resolution microstructure of 50%/2 h, (f,g) Fourier transform map.

3.3. Elastic Modulus

Figure 8 shows the elastic modulus of TNZ-7Ag aged at 600 °C for 0.5–2 h after 50% pre-deformation. After the pre-deformation, the elastic modulus of the material decreased to 57 GPa. After being aged for 0.5 h, the elastic modulus increased to 65 GPa due to $\beta \rightarrow \alpha''$ -phase transition behavior and reached a maximum value of 75 GPa after 1 h of aging. After that, as the $\beta \rightarrow \alpha''$ -phase transition process tended to stabilize, $\alpha' \rightarrow \alpha''$ became the main phase transition process, and the elastic modulus was maintained at about 76 GPa, which was lower than that of the samples without pre-deformation treatment of TNZ-7Ag and Ti-13Nb-13Zr [10]. However, there was α -phase nucleation in the process of $\alpha'' \rightarrow \alpha + \text{Ti}_2\text{Ag}$. Since the aging time was short, the α phase has not grown significantly and the overall phase composition was $\beta + \alpha''$, so the elastic modulus was maintained at a low level.

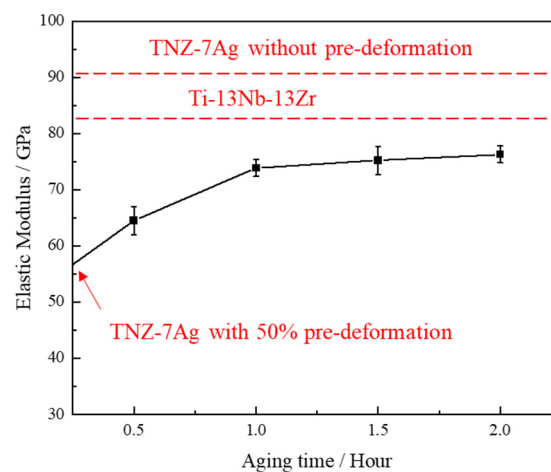


Figure 8. The elastic modulus of TNZ-7Ag with 50% pre-deformation and aging for 0.5–2 h, TNZ-7Ag without pre-deformation and Ti-13Nb-13Zr (data from ref. [11]) listed in red.

3.4. Corrosion Resistance

Figure 9 shows the Tafel results of TNZ-7Ag with 50% pre-deformation + aging at 600 °C for 0.5–2 h. After the pre-deformation, the corrosion current density of TNZ-7Ag decreased gradually with the extension of the aging time, which indicates that the corrosion resistance was enhanced. Compared to the corrosion current density of TNZ-7Ag without pre-deformation, TNZ-7Ag samples with more Ti₂Ag phase could obtain stronger corrosion resistance.

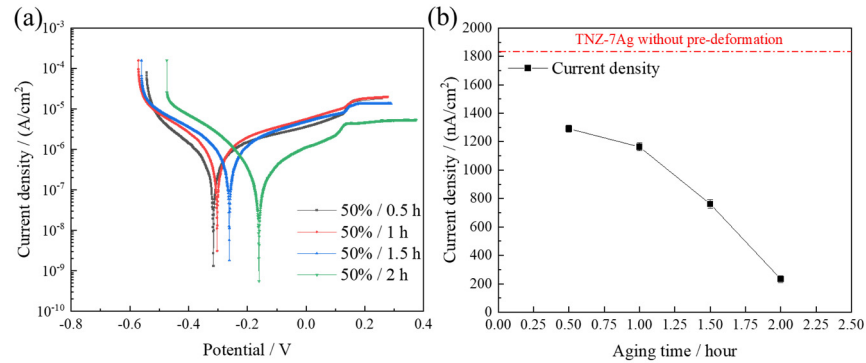


Figure 9. Tafel curves and data results of TNZ-7Ag with 50% pre-deformation and aged at 600 °C for 0.5–2 h. (a) Tafel curves, (b) corrosion current density.

Figure 10 shows the results of Ag ion concentration and Ag ion release rate after up to 7 days of immersion in SBF solution. From Figure 10a, the Ag ion release concentrations of TNZ-7Ag treated by different methods did not differ much, and all of them remained at a low level. And according to the Ag ion release rate converted from the concentration (Figure 10b), it can be known that the Ag ion release rate was higher in the initial stage and remained at a similar level in the first 3 days, while after 7 days of immersion, the rate decreased to 0.5 $\mu\text{g}/(\text{L}\cdot\text{d})$, which was due to the dense and thickened passivation film formed by long-term immersion.

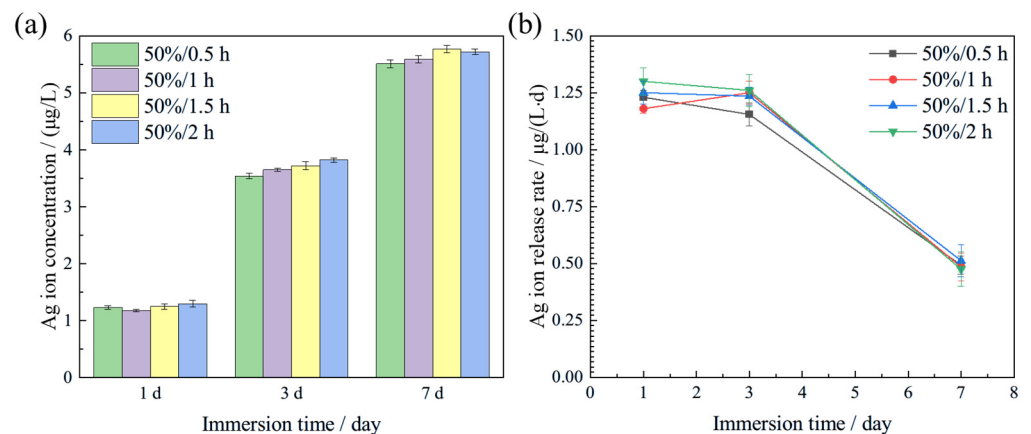


Figure 10. Ag ion concentration and release rates from TNZ-7Ag alloys with 50% pre-deformation and aged for 0.5–2 h after 1 day, 3 days, and 7 days of immersion. (a) Ag ion concentration, (b) Ag ion release rate.

3.5. Antibacterial Properties

Figure 11 shows the results of antibacterial properties of TNZ-7Ag after different aging durations. From the bacterial colony counts, it can be visualized that the antibacterial properties were significantly enhanced as the aging time increased. From the corresponding antibacterial rates, it can be found that the antibacterial rate was about 80% after aging for 0.5 h. At this time, the amount of Ti₂Ag precipitated was not enough to provide the

optimal antimicrobial effect, whereas the antibacterial rate of the material was maintained at more than 95% after aging for more than 1 h due to the formation of the large number of Ti_2Ag phases.

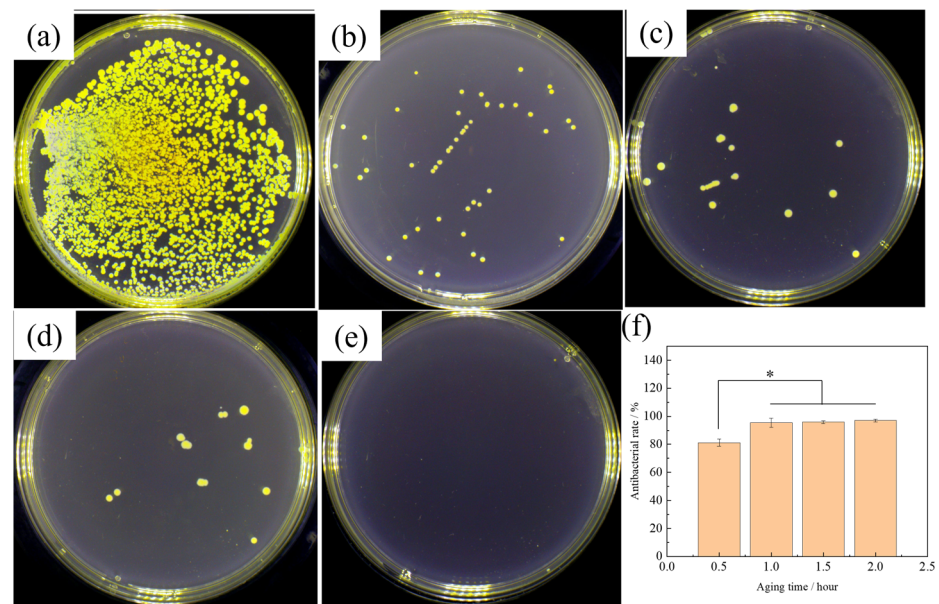


Figure 11. Bacterial colonies on TNZ-7Ag with 50% deformation + 600 °C aging for 0.5–2 h and the antibacterial rate. (a) cp Ti, (b) 0.5 h, (c) 1 h, (d) 1.5 h, (e) 2 h, (f) antibacterial rate (* $p > 0.05$, $n = 3$).

3.6. Cytotoxicity

Figure 12 shows the cytotoxicity test results of MC3T3-E1 cells after 1, 3, and 7 days of co-culture with TNZ-7Ag extract. Figure 12a shows the OD values obtained after co-culturing, from which TNZ-7Ag extract did not exhibit cytotoxicity in comparison with the control group (cp-Ti). According to the RGR shown in Figure 12b, all the experimental groups showed an RGR higher than 75%, which suggests that the experimental samples exhibited no cytotoxicity to MC3T3-E1 cells.

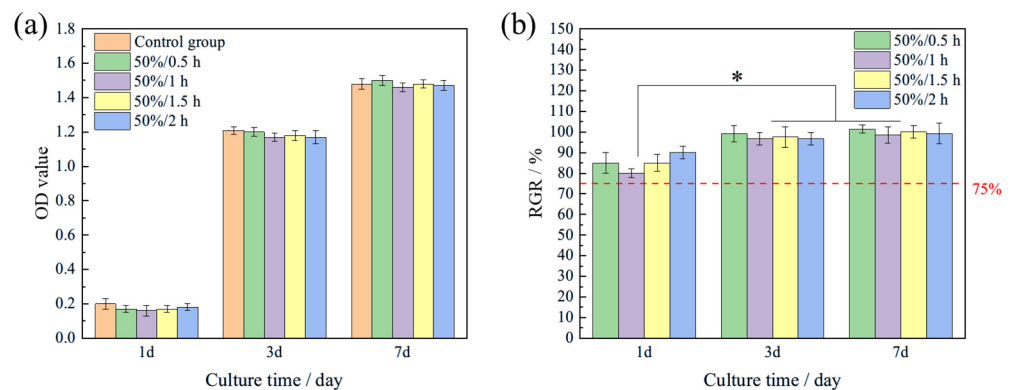


Figure 12. The OD value and relative growth rate (RGR) of MC3T3-E1 with the extracts of different samples after 1 day, 3 days, and 7 days of culture. (a) OD values, (b) RGR (* $p > 0.05$, $n = 3$).

4. Discussion

4.1. Effect of Pre-Deformation + Aging on the Microstructure

In this study, TNZ-7Ag was cold rolled with 20–50% deformation reduction. After the cold rolling, α'' martensite appeared in the alloy and the width of the martensite rose with increasing deformation. At 50% deformation, there was an obvious twinned structure according to SEM results. TEM observation suggests that two types of α'' phases were

formed in TNZ-7Ag, i.e., primary α'' M and secondary α'' T. Twinning was found in the secondary α'' T. In addition, spinodal decomposition was found in TNZ-7Ag, which formed Ag-rich areas. All these results suggest that a large amount of α'' M phase and twins were obtained in the material after 50% deformation.

The effect of the primary α'' M and twins on the aging precipitation behavior of Ti_2Ag was clarified by microstructure observation on the 50%/0.5–2 h TNZ-7Ag. During the aging, these α'' M phases were transformed into Ag-poor α'' phases and Ti_2Ag phase particles. At the same time, α phase with the size of about 1 μm formed in the residual β phase. TEM observations showed that after the aging treatment, Ti_2Ag phase precipitated in large quantities along the twinned martensite α'' T, forming clusters with sizes of 200–500 nm, which increased the size of Ti_2Ag phases by about 150% compared to that in TNZ-7Ag without pre-deformation [11]. As a summary, the primary α'' M and secondary α'' T induced by the pre-deformation successfully increased the amount and size of the Ti_2Ag phase.

4.2. Antibacterial Properties and Elastic Modulus

The antibacterial activity of Ti_2Ag -phase particles is related to both their number and size. Fu et al. [15] showed that larger-sized Ti_2Ag had stronger antibacterial properties compared to smaller Ti_2Ag phases, and high ROS expression was observed on the surface of the alloys containing Ti_2Ag phases, suggesting that Ti_2Ag phases can kill bacteria by contacting the surface of the bacteria to cause oxidative stress [22,23]. Chen et al. [2] also reported that the antibacterial properties of Ti-Ag alloys were enhanced with the rise in the size and the number of Ti_2Ag phases. In this study, the antibacterial rate of TNZ-7Ag was 80% at the beginning of the aging process (0.5 h) and reached >95% when the aging time reached 1 h due to the pairs of Ti_2Ag -phase particles formed at twin boundaries, which significantly increased the size and number of the Ti_2Ag phases. However, the effect of aging time prolongation was no longer obvious after 1–2 h, and the antibacterial rates were retained at 95%, which indicates that the amount of Ti_2Ag phase reached the level of providing sufficient antibacterial effect after 1 h of aging treatment. In contrast, the numbers and sizes of TNZ-7Ag without pre-deformation were much less than in this study, while the antibacterial rate was only 30–40% after being aged at 600 °C for 2 h [11]. This strongly demonstrates that the α'' M and α'' T could enhance the antibacterial ability of TNZ-7Ag after aging by increasing the number and size of Ti_2Ag particles.

Another aspect of interest in this study is the effect of the α'' M and twins induced by pre-deformation on the elastic modulus of TNZ-7Ag during the aging process, which is mainly influenced by the phase composition of the titanium alloys. For the phases present in this study, the order of elastic modulus is $E_\alpha > E_{\alpha''} > E_\beta$ [24]. After 50% pre-deformation, the phase composition was $\beta + \alpha''$, which could effectively decrease the elastic modulus. As a result, the elastic modulus of TNZ-7Ag was 55 GPa. After aging at 600 °C, the elastic modulus increased due to the phase transformation $\beta \rightarrow \alpha'' + \alpha$. However, when the aging time was extended to 1–2 h, the elastic modulus reached a maximum of about 75 GPa, which means the existence of α'' phase limits the precipitation of α phase. Microstructure observation showed that although α -phase precipitation was observed at 1.5 h of aging, the increases in the number and size were not obvious, which was because the α'' M and α'' T hindered the growth of the α -phase grains. This phenomenon of the elastic modulus not increasing with aging time is like the Elinvar effect [25]. Hao et al. [16] reported that the temperature coefficient of elastic modulus can be varied continuously from positive (zero by the Elinvar effect) to negative in spinodal decomposition Ti-Nb-based alloys, which is achieved by modulating the nanoscale composition of the $\beta + \alpha''$ phase. Similar results were found in this study. In this study, the synergistic effect of the solute element clustering of α'' M and the twin boundaries of α'' T prevent the increase in the elastic modulus by limiting the growth of the α phase with high elastic modulus and maintain the $\beta + \alpha''$ phase with low elastic modulus, which provides a reference for the development of novel low-elastic-modulus antibacterial titanium alloys.

4.3. Corrosion Resistance and Cytotoxicity

Corrosion resistance and cytotoxicity are critical issues that must be considered in the development of biomedical materials. Low Ag concentration does not show cytotoxicity to osteoblasts [26]. The concentration of Ag ions was influenced by corrosion resistance, with higher stability in the alloy resulting in lower concentrations of released Ag ions in the SBF environment. Analysis of the corrosion current density obtained from Tafel curves revealed a decrease in the corrosion current density of TNZ-7Ag with prolonged aging time. This decrease indicates an enhancement in corrosion resistance, attributed to the increased presence of the Ti₂Ag phase, which augments the inert component on the alloy surface. It can be found that the Ag ion release was not sensitive to the precipitation of Ti₂Ag phase corresponding to the analysis of the Ag ion release results, which was because the bactericidal effect of Ti₂Ag came from the contact sterilization, which did not decompose in the SBF solution, and a dense passivation film was encapsulated on the alloy surface, which effectively blocked the ion release pathway. In addition, Zheng et al. [27] reported that the selective dissolution of Ti on the surface of Ag-containing Ti alloys during immersion could increase the percentage of Ag on the surface, which in turn improved the long-term corrosion resistance. Tweden et al. [28] showed that the concentration of Ag ion reached more than 1200 µg/L to cause a cytotoxicity, and the amount of Ag ion release in this study was much lower than this value. The corresponding cytotoxicity test also showed that there was no cytotoxicity of TNZ-7Ag with pre-deformation + aging in this study.

5. Conclusions

1. Two types of α'' phase, $\alpha''M$ and $\alpha''T$, were successfully introduced to TNZ-7Ag by a deformation at room temperature.
2. The $\alpha''M$ and $\alpha''T$ induced by pre-deformation effectively increased the size and number of Ti₂Ag phases during the following aging and improved the antibacterial properties.
3. The solute element clustering and the twin boundaries limited the nucleation and growth of the α phase and kept a low elastic modulus during the aging treatment at 600 °C.
4. The TNZ-7Ag with high antibacterial properties and low elastic modulus has been successfully obtained by pre-deformation and aging treatment, and it also exhibits excellent corrosion resistance and cytocompatibility.

Author Contributions: Conceptualization, E.Z. and D.C.; methodology, D.C.; software, D.C. and J.W.; validation, D.C., J.W. and X.X.; formal analysis, D.C. and J.W.; investigation, D.C. and X.X.; resources, E.Z.; data curation, D.C. and X.X.; writing—original draft preparation, D.C.; writing—review and editing, E.Z. and L.Y.; visualization, D.C. and J.W.; supervision, L.Y. and E.Z.; project administration, L.Y. and E.Z.; funding acquisition, E.Z. All authors have read and agreed to the published version of the manuscript.

Funding: The authors would like to acknowledge the financial support from the National Key R&D Program of China (No. 2022YFE0122800), National Natural Science Foundation of China (No. 32371390).

Data Availability Statement: The original contributions presented in the study are included in the article, further inquiries can be directed to the corresponding author.

Conflicts of Interest: The authors declare no conflict of interest.

References

1. Liang, Y.; Song, Y.; Wang, L.; Wei, C.; Zhou, X.; Feng, Y. Research progress on antibacterial activity of medical titanium alloy implant materials. *Odontology* **2023**, *111*, 813–829. [[CrossRef](#)] [[PubMed](#)]
2. Chen, M.; Yang, L.; Zhang, L.; Han, Y.; Lu, Z.; Qin, G.; Zhang, E. Effect of nano/micro-Ag compound particles on the bio-corrosion, antibacterial properties and cell biocompatibility of Ti-Ag alloys. *Mater. Sci. Eng. C* **2017**, *75*, 906–917. [[CrossRef](#)] [[PubMed](#)]
3. Li, M.; Ma, Z.; Zhu, Y.; Xia, H.; Yao, M.; Chu, X.; Wang, X.; Yang, K.; Yang, M.; Zhang, Y.; et al. Toward a Molecular Understanding of the Antibacterial Mechanism of Copper-Bearing Titanium Alloys against *Staphylococcus aureus*. *Adv. Healthc. Mater.* **2016**, *5*, 557–566. [[CrossRef](#)] [[PubMed](#)]

4. Shao, H.; Zhang, T.; Gong, Y.; He, Y. Silver-Containing Biomaterials for Biomedical Hard Tissue Implants. *Adv. Healthc. Mater.* **2023**, *12*, 2300932. [[CrossRef](#)] [[PubMed](#)]
5. Marczewski, M.; Jurczyk, M.; Pecyna, P.; Ratajczak, M.; Gajecka, M.; Jurczyk, M.U. The Effect of 45S5 Bioglass and Ag, Cu, or Zn Addition on the Crystal Structure, Properties, and Antibacterial Effect of Bulk Ti₂₃Zr₂₅Nb Biocomposites. *Metals* **2020**, *10*, 1115. [[CrossRef](#)]
6. Aziz, N.; Faraz, M.; Sherwani, M.A.; Fatma, T.; Prasad, R. Illuminating the Anticancerous Efficacy of a New Fungal Chassis for Silver Nanoparticle Synthesis. *Front. Chem.* **2019**, *7*, 65. [[CrossRef](#)] [[PubMed](#)]
7. Fan, L.; Chen, S.; Yang, M.; Liu, Y.; Liu, J. Metallic Materials for Bone Repair. *Adv. Healthc. Mater.* **2024**, *13*, 2302132. [[CrossRef](#)] [[PubMed](#)]
8. Takizawa, T.; Nakayama, N.; Haniu, H.; Aoki, K.; Okamoto, M.; Nomura, H.; Tanaka, M.; Sobajima, A.; Yoshida, K.; Kamanaka, T.; et al. Titanium Fiber Plates for Bone Tissue Repair. *Adv. Mater.* **2018**, *30*, 1703608. [[CrossRef](#)]
9. Mohammed, M.T.; Khan, Z.A.; Siddiquee, A.N. Beta titanium alloys: The lowest elastic modulus for biomedical applications: A review. *Int. J. Chem. Mol. Nucl. Mater. Metall. Eng.* **2014**, *8*, 726–731.
10. Liang, S. Review of the Design of Titanium Alloys with Low Elastic Modulus as Implant Materials. *Adv. Eng. Mater.* **2020**, *22*, 2000555. [[CrossRef](#)]
11. Cai, D.; Yu, Z.; Yang, L.; Nie, J.-J.; Wang, R.; Chen, D.; Zhang, E. Effect of Ag content on the microstructure and antibacterial activity of biomedical titanium alloy Ti-13Nb-13Zr-xAg (x = 7,10 wt%). *Mater. Lett.* **2024**, *354*, 135389. [[CrossRef](#)]
12. Cui, S.; Liu, S.; Nie, J.; Chen, D.; Wu, X.; Qin, G.; Zhang, E. Design and preparation of a biomedical titanium alloy with low elastic modulus and high antibacterial property based on Ti-Mo-Ag system. *J. Alloys Compd.* **2022**, *908*, 164639. [[CrossRef](#)]
13. Hussein, M.A.; Kumar, A.M.; Azeem, M.A.; Sorour, A.A.; Saravanan, S. Ti-30Nb-3Ag alloy with improved corrosion resistance and antibacterial properties for orthopedic and dental applications produced by mechanical alloying. *J. Mech. Behav. Biomed. Mater.* **2023**, *142*, 105851. [[CrossRef](#)] [[PubMed](#)]
14. Hussein, M.A.; Azeem, M.A.; Kumar, A.M.; Saravanan, S.; Ankah, N.; Sorour, A.A. Design and processing of near- β Ti-Nb-Ag alloy with low elastic modulus and enhanced corrosion resistance for orthopedic implants. *J. Mater. Res. Technol.* **2023**, *24*, 259–273. [[CrossRef](#)]
15. Fu, S.; Zhang, Y.; Qin, G.; Zhang, E. Antibacterial effect of TiAg alloy motivated by Ag-containing phases. *Mater. Sci. Eng. C* **2021**, *128*, 112266. [[CrossRef](#)] [[PubMed](#)]
16. Gong, D.; Wang, H.; Wang, Q.; Li, S.; Lin, K.; Wang, Y.; Yang, R.; Hao, Y. Tuning temperature coefficient of elastic modulus by heat treatment in a compositionally-modulated Ti-Nb-based alloy. *Scr. Mater.* **2023**, *227*, 115275. [[CrossRef](#)]
17. Ma, X.; Chen, Z.; Xiao, L.; Luo, S.; Lu, W. Stress-induced martensitic transformation in a β -solution treated Ti-10V-2Fe-3Al alloy during compressive deformation. *Mater. Sci. Eng. A* **2021**, *801*, 140404. [[CrossRef](#)]
18. GB/T 31544-2015; Test Method for Elastic Properties of Glass at High Temperatures—Impulse Excitation of Vibration. Industrial Glass and Special Glass: Beijing, China, 2015; pp. 1–5.
19. Bohner, M.; Lemaître, J. Can bioactivity be tested in vitro with SBF solution? *Biomaterials* **2009**, *30*, 2175–2179. [[CrossRef](#)]
20. GB/T 16886. 12-2005; Biological Evaluation of Medical Devices—Part 12: Sample Preparation and Reference Materials. Industrial Glass and Special Glass: Beijing, China, 2015; pp. 1–9.
21. Thangaraju, P.; Varthya, S.B. ISO 10993: Biological evaluation of medical devices. In *Medical Device Guidelines and Regulations Handbook*; Springer: Cham, Switzerland, 2022; pp. 163–187.
22. Mittler, R.; Vanderauwera, S.; Suzuki, N.; Miller, G.; Tognetti, V.B.; Vandepoele, K.; Gollery, M.; Shulaev, V.; Van Breusegem, F. ROS signaling: The new wave? *Trends Plant Sci.* **2011**, *16*, 300–309. [[CrossRef](#)]
23. Su, H.-L.; Chou, C.-C.; Hung, D.-J.; Lin, S.-H.; Pao, I.C.; Lin, J.-H.; Huang, F.-L.; Dong, R.-X.; Lin, J.-J. The disruption of bacterial membrane integrity through ROS generation induced by nanohybrids of silver and clay. *Biomaterials* **2009**, *30*, 5979–5987. [[CrossRef](#)]
24. Ruzic, J.; Emura, S.; Ji, X.; Watanabe, I. Mo segregation and distribution in Ti-Mo alloy investigated using nanoindentation. *Mater. Sci. Eng. A* **2018**, *718*, 48–55. [[CrossRef](#)]
25. He, Q.F.; Wang, J.G.; Chen, H.A.; Ding, Z.Y.; Zhou, Z.Q.; Xiong, L.H.; Luan, J.H.; Pelletier, J.M.; Qiao, J.C.; Wang, Q.; et al. A highly distorted ultraelastic chemically complex Elinvar alloy. *Nature* **2022**, *602*, 251–257. [[CrossRef](#)] [[PubMed](#)]
26. Harges, J.; Streitburger, A.; Ahrens, H.; Nusselt, T.; Gebert, C.; Winkelmann, W.; Battmann, A.; Gosheger, G. The Influence of Elementary Silver Versus Titanium on Osteoblasts Behaviour In Vitro Using Human Osteosarcoma Cell Lines. *Sarcoma* **2007**, *2007*, e26539. [[CrossRef](#)]
27. Zhang, B.B.; Zheng, Y.F.; Liu, Y. Effect of Ag on the corrosion behavior of Ti-Ag alloys in artificial saliva solutions. *Dent. Mater.* **2009**, *25*, 672–677. [[CrossRef](#)] [[PubMed](#)]
28. Tweden, K.S.; Cameron, J.D.; Razzouk, A.J.; Holmberg, W.R.; Kelly, S.J. Biocompatibility of silver-modified polyester for antimicrobial protection of prosthetic valves. *J. Heart Valve Dis.* **1997**, *6*, 553–561. [[PubMed](#)]

Disclaimer/Publisher’s Note: The statements, opinions and data contained in all publications are solely those of the individual author(s) and contributor(s) and not of MDPI and/or the editor(s). MDPI and/or the editor(s) disclaim responsibility for any injury to people or property resulting from any ideas, methods, instructions or products referred to in the content.